Biosensors and Bioelectronics 205 (2022) 114116

Contents lists available at ScienceDirect

Biosensors and Bioelectronics

journal homepage: www.elsevier.com/locate/bios

Three-dimensional hierarchical plasmonic nano-architecture based label-free surface-enhanced Raman spectroscopy detection of urinary exosomal miRNA for clinical diagnosis of prostate cancer

Woo Hyun Kim [a,1], Jong Uk Lee [a,b,1], Myeong Jin Jeon [a], Kyong Hwa Park [c], Sang Jun Sim [a,*]

[a] Department of Chemical and Biological Engineering, Korea University, 145, Anam-ro, Seongbuk-gu, Seoul, 02841, Republic of Korea
[b] Department of Chemical Engineering, Sunchon National University, 225 Jungang-ro, Suncheon, Jeollanam-do, Republic of Korea
[c] Division of Oncology/Hematology, Department of Internal Medicine, Korea University College of Medicine, Seoul, 02841, South Korea

ARTICLE INFO

Keywords:
Surface-enhanced Raman scattering (SERS)
Exosomal miRNA
Label-free detection
Prostate cancer
Urine
Clinical diagnosis
3D hierarchical nanostructure

ABSTRACT

The urinary exosomal miRNAs are recently emerging prostate cancer (PC)-associated biomarkers for the early-stage diagnosis and prognosis due to their non-invasiveness, inherent stability and the representation of the status of the originated cells. However, developing a urinary exosomal miRNA detection method with high accuracy is challenging because of the low abundance and high sequence homology of miRNAs. Herein, we present a quantitative and label-free miRNA sensing platform using surface-enhanced Raman scattering (SERS) based on three-dimensional (3D) hierarchical plasmonic nano-architecture to detect urinary exosomal miRNAs. This hierarchical nanostructure is constructed by self-assembly between target-complementary DNA probes-conjugated gold nanoparticles and head-flocked gold nanopillars in the presence of the target miRNAs, creating numerous 3D plasmonic hot-spots inducing exceedingly high amplification of SERS signals. This 3D SERS biosensor achieved ~10 aM detection limits for the target miRNAs (miR-10a and miR-21), which is over 1000-fold more sensitive than previously reported miRNA sensors without the requirement of any labelling or pre-treatment steps. Finally, the clinical validation using urinary samples revealed that our 3D SERS sensor discriminates PC patients from healthy control with high diagnostic accuracy (0.93) based on the differential expression level of urinary exosomal miRNAs. These outputs demonstrate that our SERS sensor based on 3D hierarchical nano-architecture can offer facile, accurate and rapid methods to measure miRNA expression and is helpful for the diagnosis of various diseases.

1. Introduction

Prostate cancer (PC) is the second most frequent malignancy and the fifth major cause of cancer-related deaths among males globally (Monn et al., 2016; Valentino et al., 2017). For the diagnosis and prognosis of PC, serum prostate-specific antigen (PSA) testing is considered the current standard (Pickles et al., 2015). However, many studies have reported that the lack of specificity and accuracy of the PSA test for PC results in a high rate of false-positive, up to 76% (Mazzucchelli et al., 2000; Thompson et al., 2006; Woolf, 1995). Certainly, this unacceptably high false-positive rate tended to increase a large number of unnecessary biopsies (Endzelins et al., 2017). Furthermore, increasing concerns have arisen considering the potential for overdiagnosis and overtreatment because of the inability to differentiate indolent from aggressive PC using PSA as a biomarker (Stuopelyte et al., 2016). Hence, there is an urgent need for the development of an accurate and reliable PC diagnosis platform using novel PC-specific biomarkers.

Recent studies have shown that tumor-derived exosome reveals insights regarding cancer pathogenesis, including tumor growth, metastasis, and tumoral angiogenesis (Azmi et al., 2013; Taylor and Gercel-Taylor, 2008; Whiteside, 2016). These nanovesicles are known to mediate intercellular communication in the tumor microenvironment and induce malignant transformation of target cells by transferring cancer-specific molecular signatures (including proteins and nucleic acids) from tumor cells to remote normal cells (Isola and Chen, 2017; Lee et al., 2020; Masyuk et al., 2013; Tickner et al., 2014). In addition,

* Corresponding author.
E-mail address: simsj@korea.ac.kr (S.J. Sim).
[1] These authors contributed equally to this work and should be considered co-first authors.

https://doi.org/10.1016/j.bios.2022.114116
Received 11 December 2021; Received in revised form 29 January 2022; Accepted 17 February 2022
Available online 25 February 2022

tumor cells are known to secrete at least 10-fold more exosomes than normal cells (Pan et al., 2019). These evidences supporting involvement in tumor progression led to intensive research on the components present in exosomes, especially the exosomal miRNAs. Exosomal miRNAs are small non-coding single-stranded RNA, modulating gene expression at post-transcriptional steps (Bartel, 2004). Due to the heterogeneity of PC (Fabris et al., 2016), urinary exosomal miRNAs have been extensively investigated as emerging biomarkers for diagnosing PC owing to remarkable stability along with possible large-scale quantities (Kim et al., 2021; Overbye et al., 2015; Rodriguez et al., 2017). Furthermore, urinary exosomal miRNA expression is directly modified in association with organ functioning for genitourinary cancer (Zang et al., 2019; Zhan et al., 2018). Among the exosomal miRNAs, exosomal miRNA-21 (miR-21) had been confirmed as an oncogene for PC, which regulates the expression of multiple tumor-related genes through p53 network to promote PC cell proliferation and invasion (Gao et al., 2016; Zhan et al., 2018). Additionally, exosomal miRNA-10a (miR-10a) has been recently revealed as an oncogenic miRNA in PC (Zimta et al., 2019) which are released from the cancer cells, inducing conversion of normal cells into a cancer stem cell (Ngalame et al., 2018). Thus, for this reason, many research groups developed miR-10a and miR-21 detection platforms for the diagnosis of PC.

Conventional methods for detection of miRNAs in blood or biofluids include Northern blotting (Varallyay et al., 2008), qRT-PCR (Varkonyi-Gasic et al., 2007; Wang and Yang, 2010), microarray (Zhao et al., 2012), and fluorescence-based techniques (Shi et al., 2012). These methods require time-consuming and lengthy protocols and high costs due to the use of fluorescent labelling. In addition, conventional methods with low sensitivity need an additional amplification process or exploit a large amount of sample for diagnosis of prostate cancer in exosome containing biofluids (ranging from aM to fM) (Campuzano et al., 2014; Labib et al., 2013). Therefore, it is urgent to develop a sensing platform having a superb performance for prostate cancer diagnosis with a simple pre-treatment process, ultra-sensitivity, high selectivity, and broad dynamic detection range. Surface-enhanced Raman scattering (SERS)-based optical biosensor exploiting noble metal substrates or nanoparticles has gathered much attention as a promising technique due to providing specific “fingerprint” spectral profiles for individual bio-analytes (protein, DNA, and RNA) adsorbed onto the roughened metal nanostructures (Abell et al., 2012; Huang et al., 2020; Langer et al., 2020; Xu et al., 2015). The signal from the metal nanostructures is amplified for 6 to 14 orders of magnitude compared with the non-enhanced Raman signal, through the localized surface plasmon resonance (Lee et al., 2015; Nguyen et al., 2016; Willets, 2009). However, the applicability of SERS is limited in complex clinical samples due to the strong background signals, especially when the concentration of the target biomolecule is extremely low (Li et al., 2013). To employ label-free SERS detection in clinical samples, developing a SERS biosensor with sufficiently high sensitivity and selectivity is essential.

3D plasmonic nanostructures can provide higher SERS effects since the incident electric field on a 3D plasmonic nanostructure is dramatically amplified at SERS active sites, which are called electromagnetic “hot-spots” via localized surface plasmon effects compared with 2D plasmonic substrates such as nanofilm, nanodot, *etc* (Wang et al. 2015, 2018). The enhancement effect enables the recognition of Raman spectral fingerprint from an individual molecule, thereby overcoming the low sensitivity and difficulty in identifying multiple analytes in conventional Raman signal (Lin et al., 2014; Wang et al., 2017). Thus, this unique property offers the ability to detect multiple miRNAs by merging the molecular fingerprint specificity and single-molecular sensitivity (Li et al., 2013).

In this paper, we present an extraordinarily sensitive SERS biosensor for the label-free and quantitative detection of PC-related exosomal miRNAs in urine samples. In this system, we fabricated a 3D hierarchical nano-architecture based on our previously developed head-flocked gold nanopillar (Lee et al., 2019) with self-assembling DNA probe-conjugated gold nanoparticles (SAP-AuNPs) for improving the detection sensitivity by significantly enhancing the SERS signal originated from miRNAs. The neighbouring gold nanopillar heads create a nanogap, and SAP-AuNPs are located in this gap and generate multiple electromagnetic hot-spots via the plasmon coupling effect. These abundant hot-spots on the hierarchical structures are capable of greatly enhancing the local electrical field, amplifying the Raman signal from miRNAs over 10^9-fold in theoretical simulation. The established 3D SERS sensor demonstrated an outstanding low limit of detection (10 aM) for multiple PC-specific exosomal miRNAs (miR-10a and miR-21) and an extensive linear range of detection from 10 aM to 100 nM, which covers the broad concentration range of urinary exosomal miRNAs (Campuzano et al., 2014). Also, this biosensor was capable of distinguishing single-base pair mismatch of target miRNAs with high specificity. Moreover, we verified that our SERS sensor can successfully recognize the variation in the exosomal miRNA expression levels in urine samples between the PC patients and healthy controls and that our miRNA detection method is applicable in the diagnosis of PC with excellent clinical accuracy (area under ROC curve (AUC) $\geq$ 0.96). Hence, we demonstrated that our 3D hierarchical substrate-based SERS biosensor provides a promising method for miRNA-based PC diagnosis and expects to be potentially used in the diagnosis and prognosis of various clinical disorders.

2. Materials and methods

2.1. Chemicals and materials

Unless otherwise specified, all chemicals used in this experiment were obtained from Sigma Aldrich Korea. The Au pellet (Ø 3 × 3 mm, 99.99%) was acquired from Shin-woo Metal (Korea). 1.5 mL DNA LoBind tubes were provided from Eppendorf. Ambion® nuclease-free water was obtained from Thermo Fisher Scientific Korea. All solutions were prepared in ultra-pure water (18.2 mΩ/cm). DNA probes and target miRNA sequences were provided from Bioneer (Korea). The total Exosome RNA Isolation kit (Invitrogen™) was obtained from Thermo Fisher Scientific (MA, USA).

2.2. Preparation of the hierarchical 3D SERS substrate

As described in our previous study, we produced the head-flocked gold nanopillar by a maskless reactive ion etching and an electron beam evaporation (Lee et al., 2019). To conjugate the DNA probes onto the nanostructure completely, we activated the thiol group of the probes using DTT according to the protocol of the manufacturer. The activated capture probe (1 μM) was mixed with the conjugation buffer containing sodium sulfate (30 mM). The substrate was incubated with the mixture for 12 h at 30 °C. After incubation, the substrate was cleansed with DI water and blow-dried with N_2. To prevent any nonspecific adsorption of other nucleic acids onto gold surfaces (Carrascosa et al., 2010), 6-mercapto-1-hexanol (MCH) monolayer was applied nanopillar substrate. The probe-conjugated substrate was incubated in MCH solution (10 μM) at room temperature for 3 h and washed with the washing buffer containing 2 × saline-sodium citrate buffer (SSC) and 0.2% SDS. The substrate was thoroughly cleansed once more and dried with N_2. For evaluation of sensitivity or specificity of the sensor, the sample was prepared by adding the target miRNA to the human serum from 1 aM to 1 μM concentrations. The substrate was then incubated at 30 °C for 12 h, followed by washing and N_2 drying. Finally, to hybridize the SAP-AuNPs with miRNAs, we incubated the substrate with the hybridization buffer containing 2 × SSC and SAP-AuNP (10 nM) in nuclease-free water for 6 h at 30 °C, followed by DI washing and N_2 drying for SERS measurement.

3. Results and discussion

3.1. Preparation and characterization of hierarchical 3D plasmonic nanostructure and SERS biosensor

To ensure the sensitivity sufficient for clinical-level detection of exosomal miRNAs with SERS, it is essential to fabricate plasmonic nanostructures with high-density plasmonic hot-spots, producing strong amplification of near-field. For this purpose, we fabricated the SERS biosensor based on self-assembling DNA probe-conjugated gold nanoparticles (SAP-AuNPs) to plasmonic head-flocked gold nanopillar SERS substrate through the intermediacy of a target urinary exosomal miRNA so as to create numerous 3D hot-spots which induces intense electromagnetic field amplification (Li et al., 2018). In the previous works, we had fabricated plasmonic gold nanopillar structures via maskless reactive ion etching of silicon wafer and electron beam evaporation (Kim et al., 2019b; Lee et al., 2019). When this elastic nanopillar structure is in Wenzel state (*i.e.*, fully wetted by the solvent), the elasto-capillary force generated between nanopillars drives the nanopillar heads to congregate and form plasmonic hot-spots across the entire surface of the substrate (Wang et al., 2018). We further applied SAP-AuNPs to form hierarchical plasmonic nanostructures, which extend the plasmonic hot-spots into 3D spaces between periodic nanopillars and SAP-AuNPs (Fig. 1), for enhancing the sensitivity of SERS sensor and improving clinical applicability (Jones et al., 2016; Li et al. 2013, 2018; Liang et al., 2017). To form the hierarchical nanostructure and to detect the miRNAs, we chose the sandwich hybridization method, which uses two half-complementary DNA probes, capture and detection probes to recognize target miRNAs for reducing false results via improving target sequence recognition in complex biofluid environment containing various interfering biomolecules (Afzalinia and Mirzaee, 2020; Goldman et al., 2013; Kim et al., 2019a). When the target miRNA is present, the SAP-AuNP functionalized with the half-complementary DNA detection probe strands confines the target miRNA in the space between AuNP and nanopillar head and forms the 3D hot-spots.

The conjugation of the DNA detection probe onto the AuNP was confirmed with the shift of UV–visible spectra and the peak information of X-ray photoelectron spectroscopy (XPS). The DNA probe having the thiol group at the end is immobilized onto the AuNP via Au–S bonding to form SAP-AuNP. As the detection probes were bound to the AuNP surface, the UV–visible spectra were red-shifted from 519 nm to 520.5 nm (Fig. S1A). Also, the presence of Au4f and S2p peaks in the XPS spectrum of SAP-AuNP signifies the creation of Au–S bonding from the immobilization of DNA onto the AuNP (Castner et al., 1996), as shown in Fig. S1B. These results indicate that the SAP-AuNP for probing the miRNAs was successfully synthesized.

To verify the enhancement effect of SAP-AuNP in the hierarchical nanostructure, a 3D finite-difference time-domain (FDTD) simulation of the structure was conducted. As described in Fig. 1, the 3D hierarchical structure was created by the hybridization of target miRNA with the capture DNA probe and the SAP-AuNP on head-flocked gold nanopillars, as observed with field-emission scanning electron microscope (FE-SEM) image (Figs. S2 and S3). The structural model was constructed from these SEM images, with two nanopillars tilted towards each other and one SAP-AuNP placed over the gap between nanopillar heads. The plasmonic hot-spots formed between SAP-AuNP and nanopillar heads would drastically amplify the Raman signal from miRNAs located in the gaps (Fig. 2A and B) (Zhang et al., 2018). The influence of the SAP-AuNP size on electric field amplification was confirmed using four different sizes of SAP-AuNPs (5, 15, 30, 50 nm size); as shown in Fig. S4, the simulation result showed that the 15-nm SAP-AuNP induced the strongest near-field enhancement in the gaps. The simulation predicted that the 15-nm SAP-AuNP would have a four times more intense SERS enhancement effect than the bare head-flocked nanopillar structure (Fig. S5). This trend can be explained by the surface curvature of the nanoparticle. As the AuNP size increases, the convexity of the particle surface is decreased, resulting in the decrease of the absorbed or inelastic scattering of light on the nanoparticle, which weakens the surface electromagnetic field and lowers the overall SERS intensity (Gullace et al., 2021; Hong and Li, 2013). In contrast, for 5 nm SAP-AuNP, the size of the AuNP is considerably small compared to the size of the gap between AuNP and nanopillar head (~8 nm, which corresponds to the length of 22-nucleotide miRNA), resulting in the absence of the near-field amplification induced by the plasmon coupling effect (Su

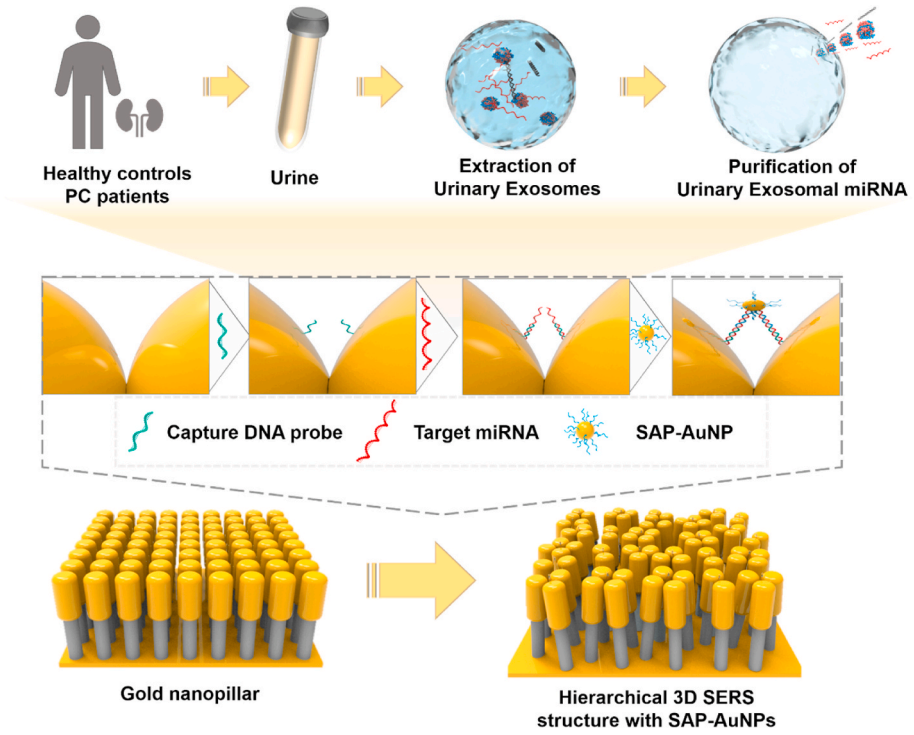

Fig. 1. Schematic for detection of urinary exosomal miRNA using hierarchical 3D SERS structure. The capture DNA probes were first immobilized onto the gold nanopillar substrates. The purified urinary exosomal miRNAs and detection probe-conjugated SAP-AuNP were then sequentially hybridized onto the substrate and formed hierarchical 3D SERS structures, inducing intense SERS signal enhancement from target miRNAs. (For interpretation of the references to color in this figure legend, the reader is referred to the Web version of this article.)

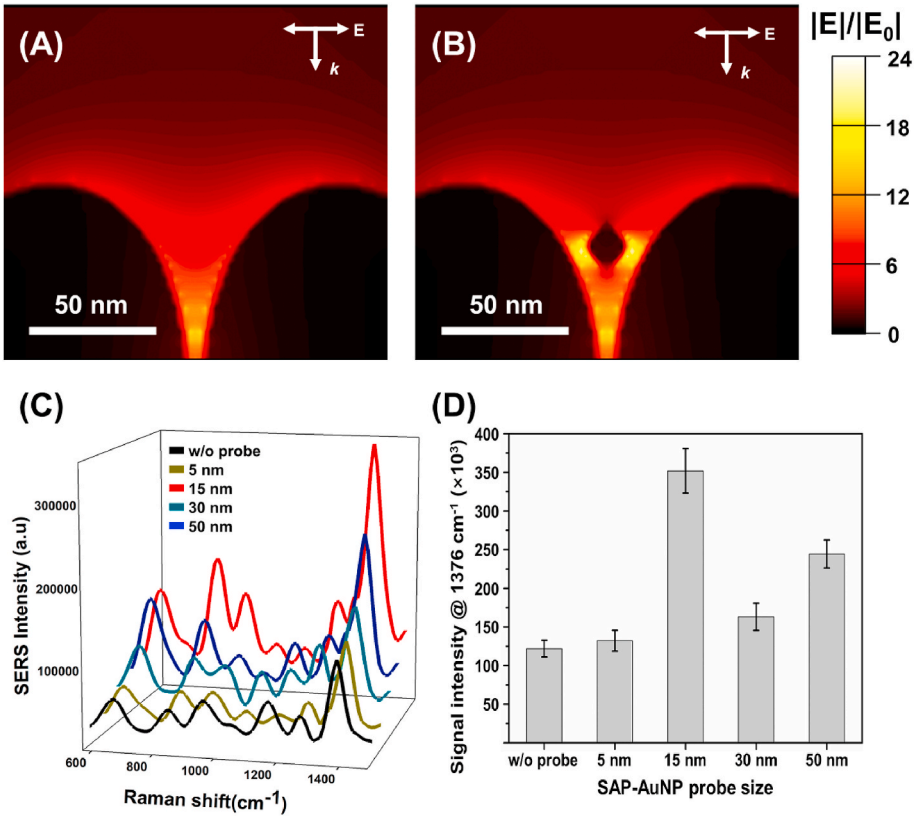

Fig. 2. Numerical simulation of the electromagnetic near-field distribution from (A) head-flocked gold nanopillar substrate without SAP-AuNP and (B) hierarchical 3D nanostructure after binding of 15-nm SAP-AuNPs. (C) Non-labelled SERS spectra graph of miR-21 and (D) SERS signal intensity at 1376 cm^{-1} (specific to miR-21) from the hierarchical nanostructures constructed with varying SAP-AuNP sizes, using 100 nM miR-21 as a model analyte. (For interpretation of the references to color in this figure legend, the reader is referred to the Web version of this article.)

et al., 2003). These results confirmed that the SAP-AuNP drastically contributes to the SERS signal enhancement and hence improves sensitivity for miRNA detection in our plasmonic nano-architecture. To assess the legitimacy of the simulation, experimental measurement of SERS signal using miR-21 was conducted. The Raman intensity at 1376 cm^{-1} peak, specific to miR-21 (Kim et al., 2019b), was compared from

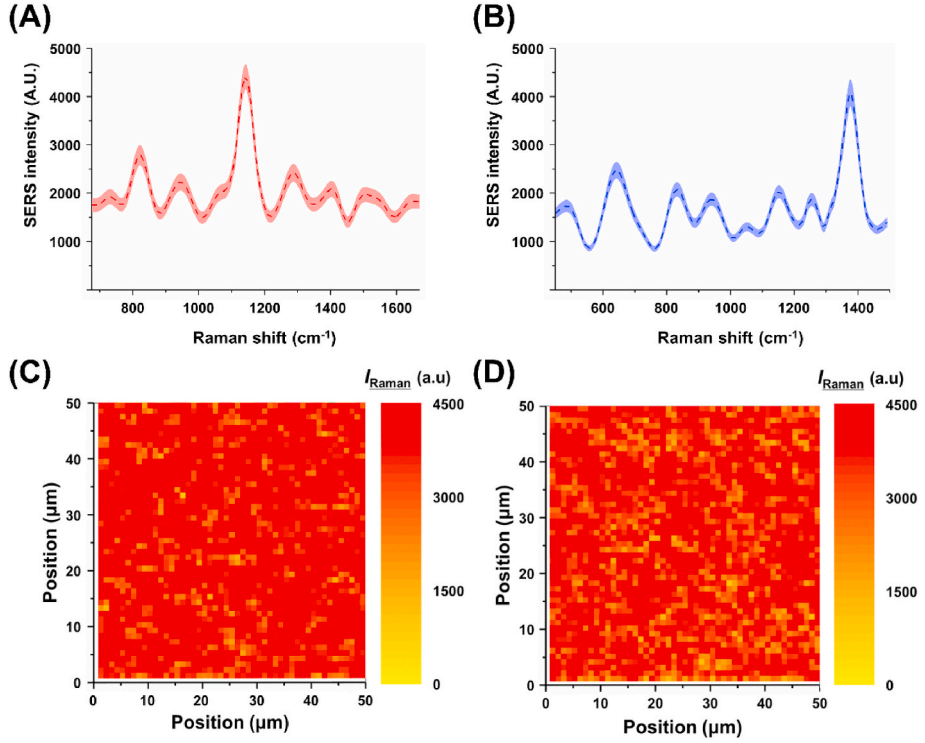

Fig. 3. Signal uniformity of hierarchical 3D SERS nanostructure-based sensor for miR-10a and miR-21. The averaged SERS spectra (dash line) and the standard deviations (colored area) of (A) miR-10a and (B) miR-21, in 50 μm × 50 μm square area (2500 points) on a single SERS sensor. Raman mapping image in a 50 μm × 50 μm square area for (C) miR-10a (1143 cm^{-1}) and (D) miR-21 (1376 cm^{-1}).

the various configuration of hierarchical nano-architecture with different nanoparticle sizes. Fig. 2C and D demonstrate that the addition of SAP-AuNP with various sizes produced the signal enhancement following the trend shown in the simulation result (Fig. S5), with the strongest signal was generated from SAP-AuNP with the size of 15 nm. The SAP-AuNP with 15 nm size exhibits 2.9-times stronger signal enhancement than the head-flocked nanopillar without the SAP-AuNP. This result indicates that the 3D plasmonic hot-spots induced on our hierarchical nanostructure generates a stronger SERS response which is consistent with other studies (Kang et al., 2010; Nguyen et al., 2016; Wang et al., 2018). This intense SERS signal amplification due to their 3D hierarchical nanostructure enables the label-free direct detection of target biomarkers including the miRNAs which exist in extremely trace amount in the biofluids.

3.2. Evaluation of miRNA sensing performance of SERS biosensor

Although the sensitivity of the SERS had been improved over time, the practical application of the SERS in the quantification of analytes had been hampered by the low reproducibility and uniformity of the results (Jarvis et al., 2008). Therefore, to exploit our 3D SERS sensor based on the hierarchical structure in the quantification of miRNAs, we evaluated the uniformity of the sensor using two miRNAs associated with PC (miR-10a and miR-21). As shown in Fig. 3A and B, the 3D SERS nanostructure-based sensor revealed high signal uniformity over mapping area (2500 points) on the substrate for both miRNAs in 100 nM concentration with small standard deviations (SD). The SERS spectra show different peak intensities because the two miRNAs have different sequence and base ratios (Kim et al., 2019b; Yao et al., 2021). Especially, miR-10a consistently produced a strong peak at 1143 cm^{-1} position, which can be attributed to Adenine C–N vibration (Zhang et al., 2020), while miR-21 showed a characteristic peak at 1376 cm^{-1} for Adenine CH_3 deformation (Kim et al., 2019b), which were also appeared in the normal Raman spectrum (Fig. S6) and were selected as the representative fingerprint peaks of each miRNA in this study. Table S2 describes more details about the SERS fingerprint peaks for both miR-10a and miR-21. The relative standard deviations (RSDs) of the characteristic peaks for miR-10a (1143 cm^{-1}) and miR-21 (1376 cm^{-1}) were 5.52 and 4.92%, respectively (Fig. S7). The signal uniformity was further verified with the mapping of Raman intensity over the square area of 50 μm × 50 μm on the SERS sensor surfaces, with a laser spot size of 1 μm diameter (Fig. 3C and D). The SERS sensor based on 3D hierarchical SERS substrate exhibited homogeneous SERS signal intensity at fingerprint peaks and spectra in response to the miRNA attachment for miR-10a and miR-21. Also, disturbances against the SERS spectrum of target miRNA had not been identified due to Raman activities of DNA probes and background SERS signal of our 3D SERS platform without target miRNA (Fig. S8). These results signify that our SERS sensor is capable of producing a uniform and reproducible SERS signal for the detection of miRNAs, which is necessary for accurate and reliable diagnostic results.

It is estimated that 2300 miRNAs are present in the human body (Alles et al., 2019), some of which are grouped as homologous miRNA family groups, with differences only one or two nucleotides among the members of a family group (Dong et al., 2014; Garcia-Rico et al., 2018; Ye et al., 2019). Due to the high sequence homology between those miRNAs, the miRNA biosensor for application in disease diagnosis necessitates selective discrimination of miRNAs with a single-nucleotide difference. To evaluate the selectivity of our SERS biosensor, we compared the SERS signal intensity from the signal intensity of the perfectly matched target miRNAs with two different single-base mismatched miRNAs (type A and type B). Type A miRNAs had single mismatch sites on the sequence complementary to the detection probes, while type B miRNAs had a single mismatch on the capture probe-complementary sequence (Table S1). The SERS signal intensities of 1143 cm^{-1} for miR-10a and 1376 cm^{-1} for miR-21 were measured and compared the fully matched with the single-base mismatched miRNAs (Fig. 4). At the same concentration (100 nM), intense SERS signals were obtained only in perfectly matched target miRNAs, whereas all single-base mismatched miRNAs (both type A and B) showed no recognizable SERS signals, indicating that single mismatch miRNAs did not react with the probe DNAs. These results represent that the 3D SERS biosensor had single-nucleotide level selectivity in the absence of the cross-reactivity and cross-hybridization with other miRNA sequences, which is necessary for the label-free detection of PC-related exosomal miRNAs.

Since the exosomes exist in extremely small amounts in the body fluids, the sensor detecting exosomal miRNAs requires ultra-high sensitivity, ideally under femtomolar detection limit (Blondal et al., 2013; Max et al., 2018; Wang et al., 2020). We investigated the limits of detection and dynamic detection ranges of our 3D SERS biosensor targeting PC-related miRNAs in the biofluid environment. Each target miRNA sample was prepared by serially diluting from 100 nM to 1 aM in human serum, and an unspecific miRNA sequence was prepared as a control (Table S1). Fig. 5A shows the SERS spectra of miRNA samples measured over concentration gradients. The Raman scattering intensities at the fingerprint peaks were plotted in Fig. 5B and C in correlation with the target miRNA concentrations. The signals at the SERS fingerprint peaks of each miRNA were detected even at deficient concentrations (~10 aM), demonstrating that the 3D SERS biosensor in this study has remarkably low detection limits for target miRNAs. Each fingerprint peak intensity for miR-10a and miR-21 showed good linear correlations of broad concentration ranges from 10 aM to 100 nM. To establish the quantitative correlation in miRNA concentration and SERS intensity, we plotted the linear regression by fitting the miRNA-specific peak intensity to target miRNA concentration in Fig. 5C. The linear regression equations were obtained as below:

$$y = 22920 \log x + 1529.6,\ R^2 = 0.968 \text{for miR} - 10a \quad (1)$$

$$y = 23039 \log x + 5118.1,\ R^2 = 0.970 \text{for miR} - 21 \quad (2)$$

where x is miRNA concentration. All the linear regressions for target miRNAs demonstrated an excellent correlation ($R^2 > 0.96$) between the representative SERS peak intensities and the logarithm of the miRNA concentrations. The evaluated detection limits were as low as 10 aM for both miR-10a and miR-21, without any chemical labelling. Compared with our formerly reported label-free SERS sensor (Kim et al., 2019b) and other amplification methods, including the fluorescence or electrochemical sensors (Chen et al., 2020; Li et al., 2020; Liu et al., 2020; Wan et al., 2020; Zhang et al., 2017), our advanced 3D SERS biosensor showed more than 1000-fold lower detection limit (Table S3). This superior detection limit of our proposed sensor is originated from the exceptional electric field enhancement induced from the 3D plasmonic hot-spots and confinement of the target miRNAs inside these 3D hot-spots of the hierarchical nano-architectures (Jones et al., 2016; Wang et al., 2018). Considering the scarcity of the urinary exosomal miRNAs in urine, as well as the large discrepancy of the concentrations between PC patients and healthy individuals (Bryzgunova et al., 2016), we anticipate that our SERS sensor having exceedingly low detection limits and wide dynamic range is feasible for the detection of the urinary exosomal miRNAs for the diagnostic application.

3.3. Clinical discrimination of PC patients from urine samples

Urinary exosomes of PC patients contain unique PC-specific contents, including miRNAs, in which exosomal miRNAs specifically are critical biomarkers in the early-stage diagnosis of PC and a personalized approach to patient prognosis and treatment. Despite the growing interest in urinary exosomal miRNA, the development of a practical urinary exosomal miRNA-based biosensor for PC diagnosis is still challenging owing to several significant drawbacks, such as the complex

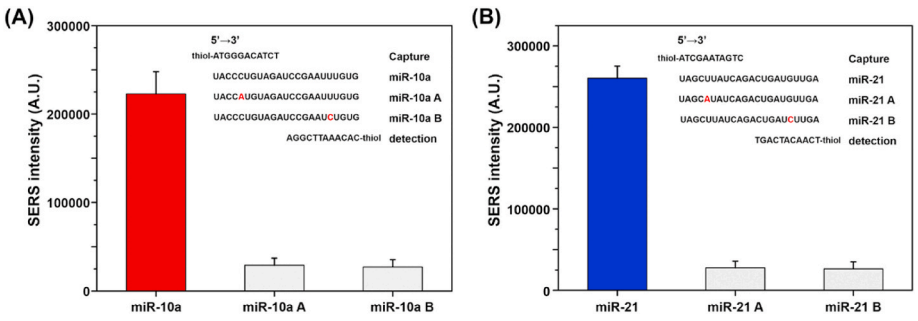

Fig. 4. Selectivity of hierarchical 3D nanostructure-based SERS sensor for detection of miR-10a and miR-21. (A) SERS intensity at 1143 cm^{-1} of miR-10a and single-mismatched sequences, and (B) SERS intensity at 1376 cm^{-1} of miR-21 and single mismatched sequences. The concentrations for each miRNA were 100 nM.

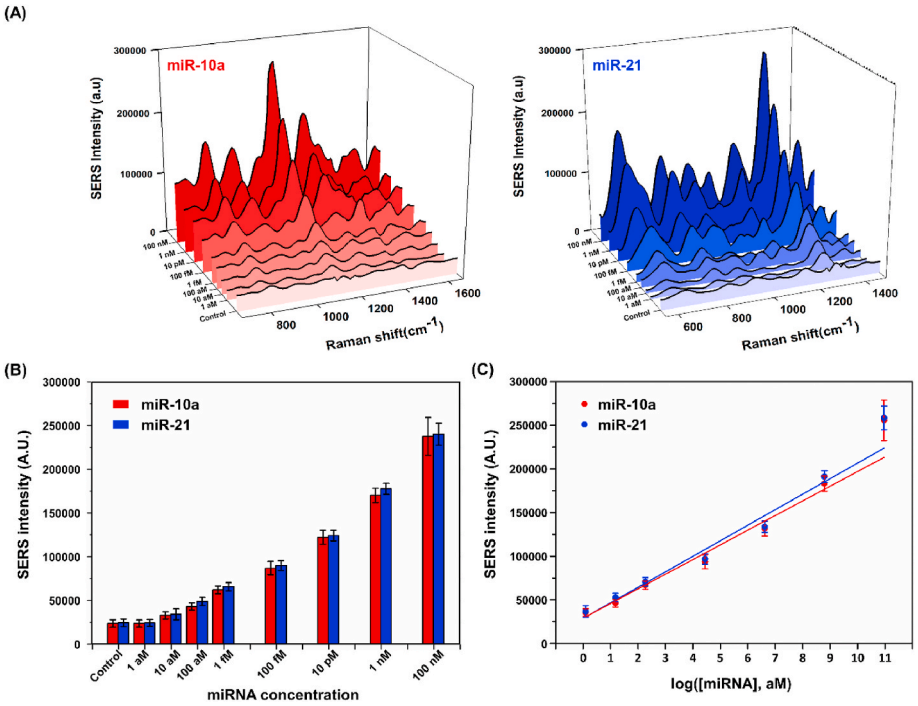

Fig. 5. Sensitivity of the hierarchical 3D SERS nanostructure-based miRNA sensor. (A) Graph of SERS spectra over concentration gradients (B) Plot of specific SERS peak intensities (1143 cm^{-1} for miR-10a and 1376 cm^{-1} for miR-21) against the miRNA concentrations in the spiked human serum sample. (C) Linear regression for the correlation between the miRNA concentration and specific peak intensity. The error bars indicate the standard deviations from 20 measurements.

composition of urine as well as low concentration of exosomes (Leung et al., 2021; Li et al., 2019). To prove the potential of our approach for PC diagnosis, our label-free 3D SERS system was applied to quantify the exosomal miRNAs in clinical urine samples acquired from ten PC patients and five healthy controls (Table S4). The purified exosomes released from the tumor cells into the urine were analyzed for surface protein expression and morphological images. The transmission electron microscopy image showed that the morphologies of the urinary exosomes were spherical shapes with diameters from 30 to 100 nm (Fig. S9A). The western blotting for the purified exosomes revealed that the exosome-associated protein markers (ALIX and CD9) were present in the urinary exosomes from both the PC patients and the healthy controls, while the non-exosomal marker (calnexin) was absent (Fig. S9B). These features are consistent with the properties of exosomes reported in other literature (Perez-Hernandez et al., 2018; Yang et al., 2017).

After extracting exosomal miRNA from urine samples, we quantified the expression levels of the target miRNA in PC patients and healthy controls using SERS spectra measured by the label-free 3D SERS biosensor (Fig. S10) and delta threshold cycles (ΔCt) value measured by the qRT-PCR. These results are presented as the box plots in Fig. 6A and B, respectively. The measurement results from both the qRT-PCR and the 3D SERS sensor revealed a higher expression level of the target miRNAs in the PC patients than in the healthy controls. This observation is in accordance with the literatures reporting elevated concentration for both miRNAs in PC (Foj et al., 2017; Worst et al., 2020). We calculated the p-value for evaluating statistically significant differences of exosomal miRNA expression levels between two clinical groups. Although both the qRT-PCR and the 3D SERS sensor showed the same tendency between miRNA concentrations and PC occurrence, qRT-PCR had p-values larger than 0.01 for both miRNAs (miR-10a: 0.12, miR-21: 0.067), whereas the p-values for the label-free SERS 3D biosensor were less than 0.01 (miR-10a: 0.0068, miR-21: 0.0035). The lower p-value stands for a statistically more significant difference between groups (Berkson, 2003; Lenzi et al., 2021). Hence, this result can be interpreted that our 3D SERS sensor shows the relation between the concentration of the miRNA and the PC occurrence more clearly than qRT-PCR and has higher clinical reliability for disease diagnosis.

The clinical sensitivity and selectivity of the PC diagnosis using the 3D SERS biosensor were further assessed using a Receiver Operating Characteristics (ROC) plot. On the ROC graph, the area under the curve

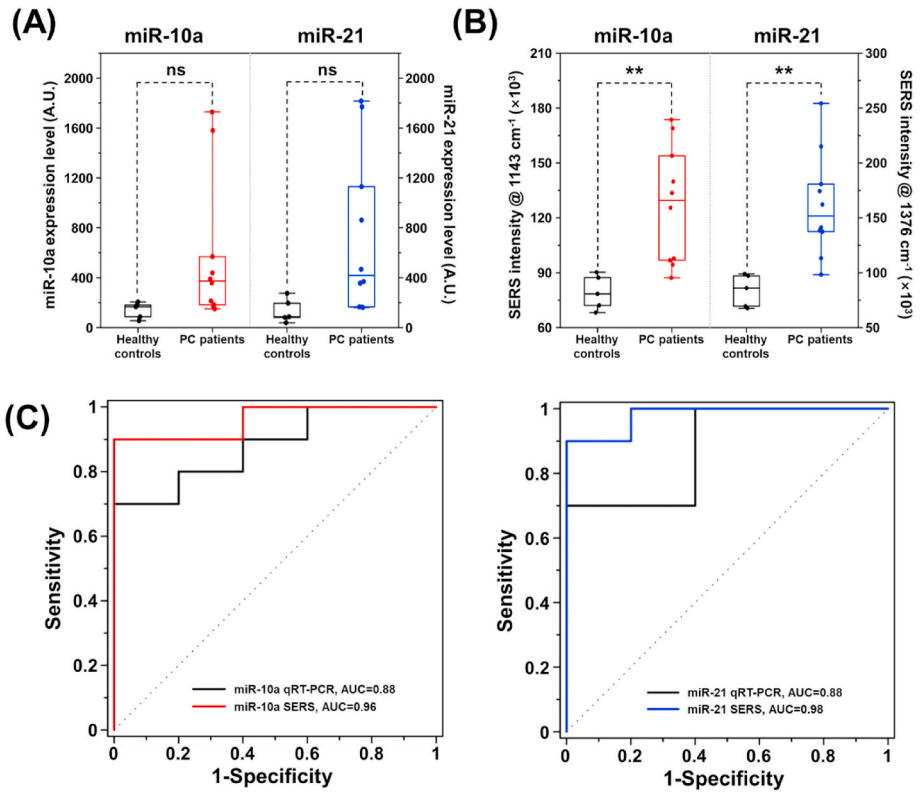

Fig. 6. Analysis of expression level of exosomal miRNAs from clinical samples regarding PC. miR-10a and miR-21 concentrations from 15 urinary samples (five healthy controls and ten PC patients) measured in (A) qRT-PCR and (B) SERS intensity from the 3D SERS sensor was depicted as the box plots. (C) The receiver operating characteristic (ROC) curve for discriminating PC patients from healthy controls using mIR-21 and miR-10a, respectively. ns, non-significant ($P \geq 0.05$); **$P < 0.01$.

(AUC) represents the diagnostic performance, where a non-significant diagnostic method has AUC near 0.5 while a value of 1 indicates perfect discrimination between positive and negative samples (Berrar and Flach, 2012). Fig. 6C displays the ROC curves of qRT-PCR and our SERS biosensor for the PC diagnosis using miR-10a and miR-21. The results showed that our 3D SERS biosensor had outstanding high sensitivity and selectivity for diagnosis of the PC patients; the AUCs of the 3D SERS biosensor for target miRNAs were 0.96 (with 95% confidence interval (CI) of 0.87–1.00) for miR-10a and 0.98 (95% CI: 0.91–1.00) for miR-21, whereas the AUCs of qRT-PCR were 0.88 (95% CI: 0.70–1.00) for miR-10a and 0.88 (95% CI: 0.71–1.00) for miR-21, respectively. The diagnosis of PC based on miRNAs using our 3D SERS biosensor achieved an accuracy of 0.93 for both miR-10a and miR-21 (Fig. S11), which were significantly improved from the accuracy of serum PSA-based PC diagnosis reported from other literatures (~50%), which has been considered insufficient for the decisive PC diagnosis (Borkowetz et al., 2020; Tubaro et al., 2008). These results demonstrate that the proposed label-free 3D SERS biosensor using the hierarchical SERS substrate had a prominent clinical potential for diagnosing PC by detecting exosome-derived urinary miRNAs.

4. Conclusion

In summary, a SERS-based, label-free biosensor was established to detect urinary exosomal miRNAs at the attomolar level sensitivity for PC diagnosis with improved accuracy. In this system, 3D hierarchical nano-architecture was constructed through the self-assembling of SAP-AuNPs with the plasmonic head-flocked gold nanopillar SERS substrate induced by the target miRNA. The uniform and abundant nanogaps in the 3D nano-architecture lead to an intense magnification of the unique SERS fingerprint peaks of the target miRNAs and result in the ultrasensitive (~10 aM) and single-nucleotide-level specific detection performance for target miRNAs. The clinical accuracy of our SERS sensor for PC diagnosis was verified by discriminating the PC patients from the healthy controls using differential expression analysis of PC-associated urinary exosomal miRNAs. Importantly, the diagnostic performance of our sensor was superior to the traditional qRT-PCR, showing the potential of our SERS-based miRNA sensor for the diagnosis of PC. Thus, we expect that our 3D SERS sensor serves as a versatile platform for detecting various disease-associated miRNAs and other trace biomarkers such as proteins or cell-free nucleic acids in biofluids, with high diagnostic fidelity. Our future works include the clinical validation of our system with larger clinical sample size and incorporation of data processing methods, including principal component analysis (PCA) for enhanced diagnostic precision.

CRediT authorship contribution statement

Woo Hyun Kim: Investigation, Methodology, Software, Data curation, Visualization, Writing – original draft, preparation. **Jong Uk Lee:** Conceptualization, Investigation, Methodology, Visualization, Writing – original draft, review & editing. **Myeong Jin Jeon:** Software, Data curation, Writing – review & editing. **Kyong Hwa Park:** Resources. **Sang Jun Sim:** Conceptualization, Supervision, Writing – review & editing, Resources, Project administration.

Declaration of competing interest

The authors declare that they have no known competing financial interests or personal relationships that could have appeared to influence the work reported in this paper.

Acknowledgment

This study was supported by grants from the National Research

Foundation of Korea (NRF) (No. NRF-2019R1A2C3009821/2020R1A5A1018052) funded by Korea government (Ministry of Science and ICT), and the Korea Health Technology R&D Project through the Korea Health Industry Development Institute (KHIDI) and Korea Dementia Research Center (KDRC), funded by the Ministry of Health & Welfare and Ministry of Science and ICT, Republic of Korea (grant number: HU21C0335). KHP acknowledges support from the National Research Foundation of Korea (NRF) under grant number of NRF-2016R1A5A1010148.

Appendix A. Supplementary data

Supplementary data to this article can be found online at https://doi.org/10.1016/j.bios.2022.114116.

References

Abell, J.L., Garren, J.M., Driskell, J.D., Tripp, R.A., Zhao, Y.P., 2012. J. Am. Chem. Soc. 134 (31), 12889–12892.
Afzalinia, A., Mirzaee, M., 2020. ACS Appl. Mater. Interfaces 12 (14), 16076–16087.
Alles, J., Fehlmann, T., Fischer, U., Backes, C., Galata, V., Minet, M., Hart, M., Abu-Halima, M., Grasser, F.A., Lenhof, H.P., Keller, A., Meese, E., 2019. Nucleic Acids Res. 47 (7), 3353–3364.
Azmi, A.S., Bao, B., Sarkar, F.H., 2013. Cancer Metastasis Rev. 32 (3–4), 623–642.
Bartel, D.P., 2004. Cell 116 (2), 281–297.
Berkson, J., 2003. Int. J. Epidemiol. 32 (5), 687–691.
Berrar, D., Flach, P., 2012. Briefings Bioinf. 13 (1), 83–97.
Blondal, T., Nielsen, S.J., Baker, A., Andreasen, D., Mouritzen, P., Teilum, M.W., Dahlsveen, I.K., 2013. Methods 59 (1), S1–S6.
Borkowetz, A., Lohse-Fischer, A., Scholze, J., Lotzkat, U., Thomas, C., Wirth, M.P., Fuessel, S., Erdmann, K., 2020. Diagnostics 10 (8), 578.
Bryzgunova, O.E., Zaripov, M.M., Skvortsova, T.E., Lekchnov, E.A., Grigor'eva, A.E., Zaporozhchenko, I.A., Morozkin, E.S., Ryabchikova, E.I., Yurchenko, Y.B., Voitsitskiy, V.E., Laktionov, P.P., 2016. PLoS One 11 (6), e0157566.
Campuzano, S., Pedrero, M., Pingarron, J.M., 2014. Anal. Bioanal. Chem. 406 (1), 27–33.
Carrascosa, L.G., Martinez, L., Huttel, Y., Roman, E., Lechuga, L.M., 2010. Eur. Biophys. J. 39 (10), 1433–1444.
Castner, D.G., Hinds, K., Grainger, D.W., 1996. Langmuir 12 (21), 5083–5086.
Chen, X., Xu, K., Li, J., Yang, M., Li, X., Chen, Q., Lu, C.H., Yang, H.H., 2020. Biosens. Bioelectron. 155, 112104.
Dong, H., Hao, K., Tian, Y., Jin, S., Lu, H., Zhou, S.F., Zhang, X., 2014. Biosens. Bioelectron. 53, 377–383.
Endzelins, E., Berger, A., Melne, V., Bajo-Santos, C., Sobolevska, K., Abols, A., Rodriguez, M., Santare, D., Rudnickiha, A., Lietuvietis, V., Llorente, A., Line, A., 2017. BMC Cancer 17, 730.
Fabris, L., Ceder, Y., Chinnaiyan, A.M., Jenster, G.W., Sorensen, K.D., Tomlins, S., Visakorpi, T., Calin, G.A., 2016. Eur. Urol. 70 (2), 312–322.
Foj, L., Ferrer, F., Serra, M., Arevalo, A., Gavagnach, M., Gimenez, N., Filella, X., 2017. Prostate 77 (6), 573–583.
Gao, Y., Guo, Y., Wang, Z., Dai, Z., Xu, Y., Zhang, W., Liu, Z., Li, S., 2016. Neoplasma 63 (4), 623–628.
Garcia-Rico, E., Alvarez-Puebla, R.A., Guerrini, L., 2018. Chem. Soc. Rev. 47 (13), 4909–4923.
Goldman, J.M., Zhang, L.A., Manna, A., Armitage, B.A., Ly, D.H., Schneider, J.W., 2013. Biomacromolecules 14 (7), 2253–2261.
Gullace, S., Montes-Garcia, V., Martin, V., Larios, D., Girelli Consolaro, V., Obelleiro, F., Calogero, G., Casalini, S., Samori, P., 2021. Small 17 (33), 2100755.
Hong, S.M., Li, X., 2013. J. Nanomater., 790323, 2013.
Huang, J.A., Mousavi, M.Z., Giovannini, G., Zhao, Y., Hubarevich, A., Soler, M.A., Rocchia, W., Garoli, D., De Angelis, F., 2020. Angew. Chem. Int. Ed. 59 (28), 11423–11431.
Isola, A.L., Chen, S., 2017. Curr. Neuropharmacol. 15 (1), 157–165.
Jarvis, R.M., Johnson, H.E., Olembe, E., Panneerselvam, A., Malik, M.A., Afzaal, M., O'Brien, P., Goodacre, R., 2008. Analyst 133 (10), 1449–1452.
Jones, S., Sinha, S.S., Pramanik, A., Ray, P.C., 2016. Nanoscale 8 (43), 18301–18308.
Kang, T., Yoo, S.M., Yoon, I., Lee, S.Y., Kim, B., 2010. Nano Lett. 10 (4), 1189–1193.
Kim, M., Ko, S.M., Lee, C., Son, J., Kim, J., Kim, J.M., Nam, J.M., 2019a. Anal. Chem. 91 (16), 10467–10476.
Kim, M., Shin, H., Moon, H.W., Park, Y.H., Park, J., Lee, J., 2021. Sci. Rep. 11 (1), 7355.
Kim, W.H., Lee, J.U., Song, S., Kim, S., Choi, Y.J., Sim, S.J., 2019b. Analyst 144 (5), 1768–1776.
Labib, M., Ghobadloo, S.M., Khan, N., Kolpashchikov, D.M., Berezovski, M.V., 2013. Anal. Chem. 85 (20), 9422–9427.
Langer, J., Jimenez de Aberasturi, D., Aizpurua, J., Alvarez-Puebla, R.A., Auguie, B., Baumberg, J.J., Bazan, G.C., Bell, S.E.J., Boisen, A., Brolo, A.G., Choo, J., Cialla-May, D., Deckert, V., Fabris, L., Faulds, K., Garcia de Abajo, F.J., Goodacre, R., Graham, D., Haes, A.J., Haynes, C.L., Huck, C., Itoh, T., Kall, M., Kneipp, J., Kotov, N.A., Kuang, H., Le Ru, E.C., Lee, H.K., Li, J.F., Ling, X.Y., Maier, S.A., Mayerhofer, T., Moskovits, M., Murakoshi, K., Nam, J.M., Nie, S., Ozaki, Y., Pastoriza-Santos, I., Perez-Juste, J., Popp, J., Pucci, A., Reich, S., Ren, B., Schatz, G. C., Shegai, T., Schlucker, S., Tay, L.L., Thomas, K.G., Tian, Z.Q., Van Duyne, R.P., Vo-Dinh, T., Wang, Y., Willets, K.A., Xu, C., Xu, H., Xu, Y., Yamamoto, Y.S., Zhao, B., Liz-Marzan, L.M., 2020. ACS Nano 14 (1), 28–117.
Lee, J.U., Kim, S., Sim, S.J., 2020. Biochip J 14 (3), 231–241.
Lee, J.U., Kim, W.H., Lee, H.S., Park, K.H., Sim, S.J., 2019. Small 15 (17), 1804968.
Lee, J.U., Nguyen, A.H., Sim, S.J., 2015. Biosens. Bioelectron. 74, 341–346.
Lenzi, E., Litti, L., de Aberasturi, D.J., Henriksen-Lacey, M., Liz-Marzan, L.M., 2021. J. Raman Spectrosc. 52 (2), 355–365.
Leung, W.H., Pang, C.C., Pang, S.N., Weng, S.X., Lin, Y.L., Chiou, Y.E., Pang, S.T., Weng, W.H., 2021. Sensors 21 (9), 3183.
Li, C.H., Zhang, C., Xu, S.C., Huo, Y.Y., Jiang, S.Z., Yang, C., Li, Z., Zhao, X.F., Zhang, S. Z., Man, B.Y., 2018. Sensor. Actuator. B Chem. 263, 408–416.
Li, M., Cushing, S.K., Zhang, J.M., Suri, S., Evans, R., Petros, W.P., Gibson, L.F., Ma, D.L., Liu, Y.X., Wu, N.Q., 2013. ACS Nano 7 (6), 4967–4976.
Li, P., Yu, X.Y., Han, W.J., Kong, Y., Bao, W.Y., Zhang, J.Q., Zhang, W.C., Gu, Y.Q., 2019. ACS Sens. 4 (5), 1433–1441.
Li, Q., Zhou, S.H., Zhang, T., Zheng, B., Tang, H.W., 2020. Biosens. Bioelectron. 150, 111866.
Liang, X., Wang, Y.S., You, T.T., Zhang, X.J., Yang, N., Wang, G.S., Yin, P.G., 2017. Nanoscale 9 (25), 8879–8888.
Lin, D., Pan, J.J., Huang, H., Chen, G.N., Qiu, S.F., Shi, H., Chen, W.W., Yu, Y., Feng, S.Y., Chen, R., 2014. Sci. Rep. 4, 4751.
Liu, G., Hong, J.J., Ma, K.F., Wan, Y., Zhang, X.T., Huang, Y.Q., Kang, K., Yang, M., Chen, J.L., Deng, S.Y., 2020. Biosens. Bioelectron. 150, 111963.
Masyuk, A.I., Masyuk, T.V., Larusso, N.F., 2013. J. Hepatol. 59 (3), 621–625.
Max, K.E.A., Bertram, K., Akat, K.M., Bogardus, K.A., Li, J., Morozov, P., Ben-Dov, I.Z., Li, X., Weiss, Z.R., Azizian, A., Sopeyin, A., Diacovo, T.G., Adamidi, C., Williams, Z., Tuschl, T., 2018. Proc. Natl. Acad. Sci. U.S.A. 115 (23), E5334–E5343.
Mazzucchelli, R., Colanzi, P., Pomante, R., Muzzonigro, G., Montironi, R., 2000. Adv. Clin. Pathol. 4 (3), 111–120.
Monn, M.F., Tatem, A.J., Cheng, L., 2016. Urol. Oncol. 34 (2), 58.e51-58.e59.
Ngalame, N.N.O., Luz, A.L., Makia, N., Tokar, E.J., 2018. Toxicol. Sci. 165 (1), 40–49.
Nguyen, A.H., Shin, Y., Sim, S.J., 2016. 85, 522-528..
Overbye, A., Skotland, T., Koehler, C.J., Thiede, B., Seierstad, T., Berge, V., Sandvig, K., Llorente, A., 2015. Oncotarget 6 (30), 30357–30376.
Pan, D., Chen, J., Feng, C., Wu, W., Wang, Y., Tong, J., Zhou, D., 2019. Int. J. Mol. Sci. 20 (2), 323.
Perez-Hernandez, J., Olivares, D., Forner, M.J., Ortega, A., Solaz, E., Martinez, F., Chaves, F.J., Redon, J., Cortes, R., 2018. J. Transl. Med. 16, 228.
Pickles, K., Carter, S.M., Rychetnik, L., 2015. BMJ Open 5 (3), e006367.
Rodriguez, M., Bajo-Santos, C., Hessvik, N.P., Lorenz, S., Fromm, B., Berge, V., Sandvig, K., Line, A., Llorente, A., 2017. Mol. Cancer 16, 156.
Shi, Z., Johnson, J.J., Stack, M.S., 2012. JAMA Oncol., 903581, 2012.
Stuopelyte, K., Daniunaite, K., Bakavicius, A., Lazutka, J.R., Jankevicius, F., Jarmalaite, S., 2016. Br. J. Cancer 115 (6), 707–715.
Su, K.H., Wei, Q.H., Zhang, X., Mock, J.J., Smith, D.R., Schultz, S., 2003. Nano Lett. 3 (8), 1087–1090.
Taylor, D.D., Gercel-Taylor, C., 2008. Gynecol. Oncol. 110 (1), 13–21.
Thompson, I.M., Chi, C., Ankerst, D.P., Goodman, P.J., Tangen, C.M., Lippman, S.M., Lucia, M.S., Parnes, H.L., Coltman, C.A., 2006. J. Natl. Cancer Inst. 98 (16), 1128–1133.
Tickner, J.A., Urquhart, A.J., Stephenson, S.A., Richard, D.J., O'Byrne, K.J., 2014. Front. Oncol. 4, 127.
Tubaro, A., De Nunzio, C., Trucchi, A., Stoppacciaro, A., Miano, L., 2008. Urology 72 (2), 340–344.
Valentino, A., Reclusa, P., Sirera, R., Giallombardo, M., Camps, C., Pauwels, P., Crispi, S., Rolfo, C., 2017. Clin. Transl. Oncol. 19 (6), 651–657.
Varallyay, E., Burgyan, J., Havelda, Z., 2008. Nat. Protoc. 3 (2), 190–196.
Varkonyi-Gasic, E., Wu, R., Wood, M., Walton, E.F., Hellens, R.P., 2007. Plant Methods 3, 12.
Wan, Z.F., Umer, M., Lobino, M., Thiel, D., Nguyen, N.T., Trinchi, A., Shiddiky, M.J.A., Gao, Y.S., Li, Q., 2020. Carbon 163, 385–394.
Wang, H.Y., Zhou, Y.F., Jiang, X.X., Sun, B., Zhu, Y., Wang, H., Su, Y.Y., He, Y., 2015. Angew. Chem. Int. Ed. 54 (17), 5132–5136.
Wang, J., Koo, K.M., Wee, E.J.H., Wang, Y.L., Trau, M., 2017. Nanoscale 9 (10), 3496–3503.
Wang, J.P., Ni, J., Beretov, J., Thompson, J., Graham, P., Li, Y., 2020. Crit. Rev. Oncol.-Hematol. 145, 102860.
Wang, X.K., Park, S.G., Ko, J., Xiao, X.F., Giannini, V., Maier, S.A., Kim, D.H., Choo, J., 2018. Small 14 (39), 1801623.
Wang, Z., Yang, B., 2010. MicroRNA Expression Detection Methods. Springer, New York.
Whiteside, T.L., 2016. Tumor-derived exosomes and their role in cancer progression. In: Makowski, G.S. (Ed.), Advances in Clinical Chemistry, vol. 74. Elsevier Academic Press Inc., San Diego, pp. 103–141.
Willets, K.A., 2009. Anal. Bioanal. Chem. 394 (1), 85–94.
Woolf, S.H., 1995. Screening for prostate cancer with prostate-specific antigen an examination of the evidence. N. Engl. J. Med. 333 (21), 1401–1405.
Worst, T.S., Previti, C., Nitschke, K., Diessl, N., Gross, J.C., Hoffmann, L., Frey, L., Thomas, V., Kahlert, C., Bieback, K., Crigna, A.T., Fricke, F., Porubsky, S., Westhoff, N., von Hardenberg, J., Nuhn, P., Erben, P., Michel, M.S., Boutros, M., 2020. Cancers 12 (1), 43.
Xu, L.J., Lei, Z.C., Li, J., Zong, C., Yang, C.J., Ren, B., 2015. J. Am. Chem. Soc. 137 (15), 5149–5154.
Yang, J.S., Lee, J.C., Byeon, S.K., Rha, K.H., Moon, M.H., 2017. Anal. Chem. 89 (4), 2488–2496.
Yao, Y.Y., Zhang, H.D., Tian, T.T., Liu, Y.X., Zhu, R.D., Ji, J., Liu, B.H., 2021. Talanta 235, 122728.

Ye, J., Xu, M., Tian, X., Cai, S., Zeng, S., 2019. J. Pharm. Anal. 9 (4), 217–226.
Zang, J., Maxwell, A.P., Simpson, D.A., McKay, G.J., 2019. Sci. Rep. 9 (1), 10900.
Zhan, F., Shen, J., Wang, R., Wang, L., Dai, Y., Zhang, Y., Huang, X., 2018. Cancer Manag. Res. 10, 4029–4038.
Zhang, F., Guo, S., Liu, Y., Chen, L., Wang, Y.X., Gao, R.X., Zhu, A.N., Zhang, X.L., Zhang, Y.J., 2018. Nanomaterials 8 (7), 493.
Zhang, H., Yi, Y., Zhou, C.H., Ying, G.Q., Zhou, X.D., Fu, C.P., Zhu, Y.F., Shen, Y.Q., 2017. RSC Adv. 7 (83), 52782–52793.
Zhang, H.D., Lai, H.S., Li, G.K., Hu, Y.F., 2020. Talanta 220, 121366.
Zhao, B.T., Jin, L., Wei, J.L., Ma, Z.L., Jiang, W.J., Ma, L.J., Jin, Y.X., 2012. IUBMB Life 64 (7), 612–616.
Zimta, A.A., Schitcu, V., Gurzau, E., Stavaru, C., Manda, G., Szedlacsek, S., Berindan-Neagoe, I., 2019. Environ. Res. 178, 108700.